

DFT+DMFT calculations of the band gap and the transmission decay rate for the transition metal monoxides MnO, FeO, CoO and NiO

Long Zhang¹, Peter Staar^{2,*}, Anton Kozhevnikov³, Yun-Peng Wang¹,
Jonathan Trinastic¹, Thomas Schulthess^{2,3}, and Hai-Ping Cheng^{1†}

¹ *Department of Physics and The Quantum Theory Project, University of Florida, Gainesville FL 32611, USA*

² *Institute for Theoretical Physics, ETH Zurich, 8093 Zurich, Switzerland and*

³ *Swiss National Supercomputing Center, ETH Zurich, 6900 Lugano, Switzerland*

We report density functional theory plus dynamical mean field theory (DMFT) calculations of the band structures for the four late transition metal monoxides, MnO, FeO, CoO and NiO, in their paramagnetic phase. From band structure calculated using an all-electron, full-potential LAPW treatment, as implemented in the modified ELK code, we construct non-interacting Hamiltonians using Wannier orbital techniques. We then calculate the Coulomb interaction U -matrices from first-principles in conjunction with the constrained random phase approximation (cRPA). The Hamiltonians and the U -matrices enable further theoretical investigations with the inclusion of strong correlation effects. The resulting self-energies from DMFT calculations are used to calculate the spectral functions and the complex band structure (CBS) of these materials. The so-called β parameters, governing the exponential decay of the transmission probability in the nonresonant tunneling regime of these oxides, are extracted from the CBS. Different model constructions are examined. We find that the obtained band gaps strongly depend on the Coulomb interaction strength. The band gaps of the model are in overall agreement with existing experiments. The value of the β parameter does not vary significantly between the two different model constructions.

I. INTRODUCTION

Motivated by the application of transition metal oxides (TMO) in modern electronics, the charge transport through TMO nanojunctions has been extensively investigated in the past 20 years, both theoretically and experimentally. A large amount of literature focuses on the non-resonant tunneling experiments in which the tunneling current decays exponentially, $I = I_0 \cdot \exp(-\beta L)$, as the length of the tunnel junction (L) increases. Although the β parameter depends on the interfacial properties between the junction and the metallic electrodes, it is mainly determined by the electronic properties of the junction material. Since a large amount of TMOs are strongly correlated electron systems, a reliable calculation of β from first principles with the inclusion of electron correlation effects is important for understanding TMO nanojunctions.

Existing studies have shown that the β parameter is related to a material's band gap, the hopping parameter t of the insulating material, and the alignment of the Fermi level in the metal electrodes with the band gap of the insulating junction^{1,2}. If one considers the bulk material as an infinitely long insulating region, the effect of electrodes is minimized and the β parameter is mostly determined by the insulator's band structure. A general way to calculate β based on band structure is to evaluate the complex band structure (CBS) rather than the real band structure (RBS). This CBS approach is particularly interesting for numerical calculation of the β because of its flexibility: the calculation can be performed either using wavefunctions or Green's functions. However, applying the CBS approach on top of the standard Kohn-Sham (KS) density functional theory (DFT) may yield wrong results for those TMOs in which strong electron correlation plays an important role. The GW approximation and hybrid density functionals have been used to account for electron localization effect in the CBS approach, and these calculations give better agreement with experimentally known β values^{1,2}. In

our study, we apply the CBS method to calculate β based on the density functional theory plus dynamical mean field theory (DMFT) results for the four late transition metal monoxides: NiO, CoO, FeO and MnO.

Although appearing to be simple compounds, the series of 3d transition metal monoxides with rock salt structure present intriguing physical properties. Early in the series, TiO and VO are metallic whereas later members, such as NiO, CoO, FeO and MnO studied in this work, show clear insulating properties and antiferromagnetic ordering. According to Zaanen, Sawatzky and Allen³, the later members are also considered to be examples of charge-transfer insulators that exhibit different behavior than a classic Mott-Hubbard insulator. In a typical charge-transfer insulator, the band gap opens between hybridized ligand p -states and transition metal d -states which form the upper Hubbard band. Not only the Hubbard U but also the charge transfer energy between d and p states determine the size of the gap. In contrast, in a classic Mott-Hubbard insulator, the band gap opens through splitting of the d orbitals by the Hubbard U . The 3d TMOs have drawn great interest in the solid state theory community due to the non-trivial description of their electronic structure and magnetic properties. It is generally accepted that the oxygen 2p and metal 4s states are occupied, and the metal 3d states are partially occupied⁴. For NiO, CoO, FeO and MnO in particular, the e_g states are partially filled and the t_{2g} are fully occupied. Density functional theory in the local density approximation (LDA) fails to provide the correct electronic and magnetic ground states due to significant electron correlation effects. For example, LDA predicts a too small band gap for the anti-ferromagnetic ground state of NiO, and an improved description of the electronic structure can be obtained by using the LDA+U method with empirical value of U ^{5,6}. Independent electron, spin-polarized DFT^{7,8} calculations have some success in describing the electronic structure of 3d metal monoxides, but in general it does not provide accurate results for

the materials that demonstrate strong electron-electron correlation.

The band gaps of these four simple materials are still an active topic of research such that they provide a test set for novel electronic structure calculation methods^{5,9,10}. It is generally accepted that the on-site Coulomb interaction among the $3d$ orbitals is strong and greater than the $3d$ bandwidth¹¹ for late transition metal oxides. We thus follow the dynamical mean-field theory approach which treats the local Coulomb interaction explicitly with a Hamiltonian that is built from a DFT ground state. Within DMFT, the Hubbard model is mapped to an impurity problem and can be solved iteratively via the numerically exact quantum Monte Carlo calculation. The four late transition monoxides, especially NiO, have been extensively studied in the DMFT community and used as benchmark material for novel computational methods^{9,10}. Although the on-site Coulomb interaction values are often used as empirical parameters in DFT+DMFT and DFT+U calculations, they can also be calculated in an *ab initio* way using the same DFT ground state via the constrained DFT or constrained random phase approximation (cRPA) methods.

In this paper, we present our investigations of strong correlation effects in the paramagnetic phase of these materials using a combined first-principles DFT and DMFT scheme. NiO, CoO, FeO and MnO exhibit antiferromagnetic order below the Neel temperature of 525K. Carrying out the calculation in the paramagnetic phase at high temperature will not cause a problem because the gap opened by electronic correlation does not depend on whether the system is magnetically ordered or not. Angle-resolved photoemission experiments (ARPES) show that passing the Neel temperature would not qualitatively alter the valence band spectrum¹². Within DFT, we first calculate the four materials' ground state band structures using the full potential linearized augmented planewave (FLAPW) method. The obtained band structures are then used to construct Hamiltonians in Wannier orbital basis. In the second step we compute Coulomb interaction matrices using the cRPA method¹³. Due to the d - p mixing in the DFT band structure, we consider two models in the cRPA calculation: the dp model, in which the Coulomb interaction is obtained by excluding both d -like bands and p -like bands from the screening, and the d - dp model, in which only the d -like bands are excluded. With the Hamiltonians and the U matrices, we finally perform DMFT calculations to get the k -resolved spectral functions and analyze the band gaps. Using the DMFT self-energy, we construct the full Green's function and use it to calculate the complex band structure (CBS) and the transmission decay constant (β).

Outline : The remainder of the article is organized as follows. Section II introduces the calculation methods, including the DMFT scheme in the DCA+ package, the cRPA based on the modified version of ELK code, and the way we obtained the β parameter from CBS. The DFT+DMFT spectral function, as well as the k -dependence of the β parameter, are described in Section III. Finally, Section IV provides conclusions. The Coulomb U matrices from cRPA, $U_{mm'}^{\sigma\bar{\sigma}}$, and $U_{mm'}^{\sigma\sigma}$, for the four materials are listed in Appendix A.

II. METHODS

II.A. DFT+DMFT method

Applications of the DFT+DMFT method to TMOs originated from the work of Peierls and Mott^{14,15}. The appropriate correlation subspace was identified as those electron states in the partially-filled, transition-metal d shell, and was associated with interactions including the on-site intra- d and inter- d interactions. For a material-specific Hubbard model construction, as presented in this work, the correlation subspace is an isolated or disentangled group of bands of d orbital character. During the past two decades, the DMFT method was developed for the Hubbard model constructed for the correlation subspace of materials' d -shell¹⁶. The successful numerical scheme is generally based on a reliable DFT ground state calculation using pseudopotential (PP) plane waves, linear muffin-tin orbitals (LMTO), projected augmented waves (PAW), or full potential linearized augmented planewave (FLAPW) methods. The most widely-adopted approach involves selecting DFT bands near the Fermi energy and fitting them to a tight-binding model using the downfolding technique applied to localized orbitals like LMTO or Wannier orbitals¹⁷⁻¹⁹. This approach should work well with TMOs, for which the near-Fermi-energy bands have a dominantly d -like character and are often not entangled with the lower p -like bands or the upper bands. Thus, a material-specific Hubbard model can be constructed. The downfolding procedure changes the basis from Bloch states to localized orbital states. For each \vec{k} point, the Bloch Hamiltonian is downfolded to $H(\vec{k})$ in the Wannier orbital basis. Through a Fourier transformation from \vec{k} space to \vec{r} space, $H(\vec{k})$ appears as t_{ij} in the first term of Eq.(1) below. $H(\vec{k})$ serves as the single-particle term. It contains contributions from the effective potential of DFT calculation that creates a double-counting issue (which is explicitly accounted for by a double-counting correction within DMFT). The Hubbard model with the Coulomb interaction on the same site can be expressed as:

$$\hat{H}_{Hub} = \hat{H}_{Kinetic} + \hat{H}_{Coulomb} \\ = \sum_{i,j,\alpha,\beta} t_{ij}^{\alpha\beta} \hat{c}_i^{\dagger} \hat{c}_j + \frac{1}{2} \sum_{i,\alpha,\beta,\gamma,\delta} U_i^{\alpha\beta\gamma\delta} \hat{c}_{i,\alpha}^{\dagger} \hat{c}_{i,\beta}^{\dagger} \hat{c}_{i,\gamma} \hat{c}_{i,\delta} \quad (1)$$

Eq.(1) is the Hamiltonian for the multi-orbital Hubbard model within second quantization²⁰. The indices i, j are site indices and $\alpha, \beta, \gamma, \delta$ are the orbital indices including spin. The values of the Coulomb interaction tensor $U_i^{\alpha\beta\gamma\delta}$ can be obtained parameter-free from the same DFT ground state using the cRPA method, which will be explained in the next section. Empirical values of $U_i^{\alpha\beta\gamma\delta}$ also have been widely used in literatures of DFT+DMFT calculations. Although computationally demanding, the cRPA method has become favorable for predicting the screened Coulomb interaction strength because of its *ab initio* feature. With the hopping parameters and Coulomb interaction in hand, the DMFT method iteratively solves the Hubbard model by mapping it to an Anderson single-impurity model. The impurity Green's function is

often expressed in the path integral formulation, with integration over Grassmann fields of the second quantization creation and annihilation operators, \hat{c}^+ and \hat{c} ,

$$G_{imp}(i_1, \tau_1; i_2, \tau_2) = - \frac{\int D[\hat{c}^+] D[\hat{c}] e^{-S[\hat{c}^+, \hat{c}]} \{\hat{c}(\tau_1) \hat{c}^+(\tau_2)\}}{\int D[\hat{c}^+] D[\hat{c}] e^{-S[\hat{c}^+, \hat{c}]}} \quad (2)$$

In Eq.(2), $D[.]$ is the standard integration measure. $S[\hat{c}^+, \hat{c}]$ is the effective action as defined in Eq.(3) below. Since this work is not dedicated to QMC solver techniques, we would refer the reader to Ref.²¹ for more detailed definitions of $D[.]$ and $S[\hat{c}^+, \hat{c}]$.

$$S[\hat{c}^+, \hat{c}] = - \int_0^\beta d\tau \int_0^\beta d\tau' \sum_{i,j} \hat{c}_i^+(\tau) \mathcal{G}_{0,ij}^{-1}(\tau - \tau') \hat{c}_j(\tau') + \int_0^\beta d\tau \hat{H}_{Coulomb}(\hat{c}^+, \hat{c}) \quad (3)$$

In Equations (2) and (3), i and τ are the site index and imaginary time. $\mathcal{G}_{0,ij}$ is the bare propagator of the Anderson impurity model. It plays a similar role as the Weiss field in classical mean-field theory. Specifically, it describes an effective field coupled to the impurity that contains all non-local information of the underlying lattice, and the lattice is considered as a reservoir of non-interacting electrons in the model. The difference from the classical Weiss field arises in its time dependence, which accounts for local dynamics.

With the effective action at hand, the impurity Green's function is completely defined, and there are several well established numerical methods to solve for the impurity Green's function. The family of quantum Monte Carlo (QMC) solvers are widely accepted and numerically exact given a sufficiently long simulation time. Here we refer readers to Ref.²² for technical details about the QMC solver. In this paper we used the single-site QMC solver implemented in the DCA+ code²³ to solve the impurity problem. The DCA+ code is a multiple purpose code package, developed by Dr.P.Staar *et al*, for studying many-body problems. It includes not only the single-site, continuous-time QMC solver (CT-QMC) but also the cluster QMC solver in the dynamic cluster approximation (DCA) framework. The cluster solver has been optimized for running on GPUs and tested using the Hubbard model applied to cuprate superconductors²⁴. A novel analytical continuation algorithm, the continuous-pole-expansion method²⁵, is included in the DCA+ package for obtaining the self-energy and impurity Green's function on the real frequency axis.

For the four materials in this paper, the correlation space consists of the five d orbitals. Our calculations are performed at inverse temperature $1/kT = 20$. The number of Monte Carlo sweeps in the QMC calculation is 10^6 in each solver run.

II.B. cRPA method

The on-site Coulomb interaction parameters are a required input for the QMC solver, as it appears in the second term

of Eq.(3). One way to calculate these parameters from first principles is the constrained Random Phase Approximation(cRPA) method, which has been well described in the literature^{13,26}. Here we summarize only the main points relevant to the current calculations. As mentioned above, the method is based on a DFT ground state calculation that includes many empty bands. One aim to get an estimate of the screened Coulomb interaction for the selected bands of interest, or an energy window. For this purpose, the particle-hole polarization between all possible pairs of occupied state and unoccupied state are taken into account in the calculation. Within the RPA, the particle-hole polarization is calculated as²⁷:

$$P_{tot}(r, r'; \omega) = \sum_i^{occ.} \sum_j^{unocc.} \psi_i^*(r) \psi_j(r') \psi_j^*(r) \psi_i(r') \times \left(\frac{1}{\omega - \varepsilon_j + \varepsilon_i + i\delta} + \frac{1}{\omega + \varepsilon_j - \varepsilon_i - i\delta} \right) \quad (4)$$

where ψ_i and ε_i are the eigenfunctions and eigenenergies of the one-particle Hamiltonian in DFT.

The selected bands of interest are often around the Fermi level, and have a uniform orbital character, for example d -like in our case. Following the convention in the literatures, we label the bands of interest or energy window as the d -space. If both the occupied state and the unoccupied state are within the d -space, then the polarization contributes to $P_d(r, r'; \omega)$. All the other pairs of occupied and unoccupied states contribute to P_r , where r stands for the rest of the bands. Thus, the total polarization is divided into two parts: $P_{tot} = P_d + P_r$. P_r is related to the partially screened Coulomb interaction¹³:

$$W_r(\omega) = [1 - \nu \cdot P_r(\omega)]^{-1} \cdot \nu \quad (5)$$

In Eq.(5), ν is the bare Coulomb interaction. The total polarization, P_{tot} , screens the bare Coulomb interaction, ν , to give the fully screened interaction W . In the same way, P_d screens W_r to give the fully screened interaction W . Thus, W_r is identified as the on-site Coulomb interaction for the bands of interest, $U(\omega) \equiv W_r(\omega)$, which has included the screening effect from the realistic environment of the material.

Our cRPA calculation is based on the partial Kohn-Sham susceptibility^{27,28}:

$$\chi_r^{KS}(r, r'; \omega) = \sum_{i,j \notin C.S.} \frac{(f_i - f_j) \psi_i^*(r) \psi_j(r') \psi_j^*(r) \psi_i(r')}{\omega - \varepsilon_j + \varepsilon_i + i\delta} \quad (6)$$

where f_i and ε_i are the occupancy and energy of the eigenstate ψ_i . The summation over band indices runs over all bands excluding the cases where both i and j are inside the correlation subspace (C.S. under the summation sign). In general, the density response function $\chi(r, r'; \omega)$ is related to the Kohn-Sham susceptibility by the following integral equation²⁹:

$$\chi(r, r'; \omega) = \chi^{KS}(r, r'; \omega) + \iint dr_1 dr_2 \chi^{KS}(r, r_1; \omega) \times \left(\frac{1}{|r_1 - r_2|} + f^{xc}(r_1, r_2; \omega) \right) \times \chi(r_2, r'; \omega) \quad (7)$$

where the f^{xc} is the functional derivative of the exchange-correlation potential with respect to the charge density, which is often neglected in the random phase approximation. Since we are considering periodic crystal structures, Eq.(7) is often written in the Fourier-transformed form where $\chi(r, r'; \omega)$ becomes $\chi(q, q'; \omega)$ with q and q' the reciprocal lattice vectors. Due to the invariance of the real space response function with respect to a shift by a lattice vector R : $\chi(r + R, r' + R; \omega) = \chi(r, r'; \omega)$, the $\chi(q, q'; \omega)$ is only nonzero when q and q' differ by a reciprocal lattice vector G . Thus one can replace q by $q + G$, replace q' by $q + G'$, and restrict q to be always within the first Brillouin zone. The Fourier-transformed form of Eq.(7) is then written as:

$$\chi_{GG'}(q, \omega) = \chi_{GG'}^{KS}(q, \omega) + \sum_{G_1 G_2} \chi_{GG_1}^{KS}(q, \omega) \times (v_{G_1+q} \delta_{G_1 G_2} + f_{G_1 G_2}^{xc}(q, \omega)) \times \chi_{G_2 G'}(q, \omega) \quad (8)$$

where $v_{G+q} = 4\pi/|G+q|^2$ is the expansion coefficient of the bare Coulomb interaction. By using the partial Kohn-Sham susceptibility $\chi_{r, GG'}^{KS}(q, \omega)$ (Fourier transform of Eq.(6)) and neglecting the f^{xc} term in Eq.(7), we reach the equation for the partial RPA density response function $\chi_r^{RPA}(q, \omega)$:

$$\chi_{r, GG'}^{RPA}(q, \omega) = \chi_{r, GG'}^{KS}(q, \omega) + \sum_{G_1} v_{G_1+q} \times \chi_{r, GG_1}^{KS}(q, \omega) \times \chi_{r, G_1 G'}^{RPA}(q, \omega) \quad (9)$$

Note that the subscript r in Eq.(9) stands for the *rest* of the bands, as same as in Eq.(5). Eq.(9) is first solved for $\chi_r^{RPA}(q, \omega)$ in the calculation. The rest calculation is based on the linear response theory³⁰, where the partially screened Coulomb interaction W_r is related to inverse dielectric function ϵ^{-1} and bare Coulomb interaction v : $W_r(r_1, r_2; \omega) = \int dr \epsilon^{-1}(r_1, r; \omega) v(r, r_2)$. The inverse dielectric function ϵ^{-1} is determined by $\epsilon^{-1}(r_1, r; \omega) = 1 + v \cdot \chi_r^{RPA}(r_1, r; \omega)$. Finally the frequency-dependent screened Coulomb interaction is computed from the partial RPA density response function and the bare Coulomb interaction:

$$W_{r, GG'}(q, \omega) = v_{G+q} \delta_{GG'} + v_{G+q} \cdot \chi_{r, GG'}^{RPA}(q, \omega) \cdot v_{G'+q} \quad (10)$$

The above calculations have been implemented in the Exciting+ code (a modified version of ELK code)²⁸, which we used for the U matrix calculations. The Wannier orbitals are constructed by projection to preserve symmetry, and no spatial localization procedure is applied.

II.C. Model Construction

The DFT band structure plots of NiO, CoO, FeO and MnO have very common features, which we illustrate using NiO as an example in Figure 1. There are five *d-like* bands around the Fermi level, which represent the partially filled *d* states of the transition metal atom. Just below them are another three bands showing *p-like* character. The *d-like* bands and *p-like*

bands are separated by a small gap of about 0.2 eV, and they are isolated from all other bands. The orbital character plot, Figure 2, shows that there is a significant weight of *d*-orbital mixed into the lower *p-like* bands. This feature is typical for the four TMOs of interest. Such a mixture poses a difficulty for an accurate model construction since it is hard to separate the *d*-orbital contribution from the lower *p-like* bands. Using only the *d*-orbital components to construct Wannier orbitals and define properly the corresponding window of excluded bands for the cRPA calculation of Coulomb interactions is not a straightforward task. If the correlation subspace, traditionally called *d*-space, is built solely on the five *d-like* bands, the *d*-*p* mixing would be mostly excluded. Instead, it is preferable to project the local orbitals to the larger window including both *d*-like and *p*-like bands, resulting in more localized Wannier orbitals. We adopt this approach throughout the paper for the single particle component of the model. Still, due to the *p*-*d* hybridization, there is some arbitrariness in the cRPA part of the calculation for screened Coulomb interactions since one cannot find a window of bands for P_d that includes all *d*-weight and exclude all *p*-weight. One choice is to exclude both *d-like* and *p-like* bands in calculating P_d and use only the *d*-*d* interaction parameters for the DMFT impurity problem, which is called the *dp* model. The other choice is to exclude only the *d-like* bands in the cRPA, and call it *d-dp* model. We have carried out cRPA calculations for both models. The resulting two sets of Coulomb U matrices are used in the subsequent DFT+DMFT calculation.

A cRPA scheme based on evaluating the weight of correlated orbitals among DFT bands has been proposed and benchmarked recently to treat the mixing feature in a more reasonable way³¹. The resulting U matrices have overall smaller values than both *d* and *d-dp* models. Since the cRPA calculation is numerically intensive and a more dedicated cRPA method study is out of the scope of this work, we did not implement and perform this new cRPA scheme.

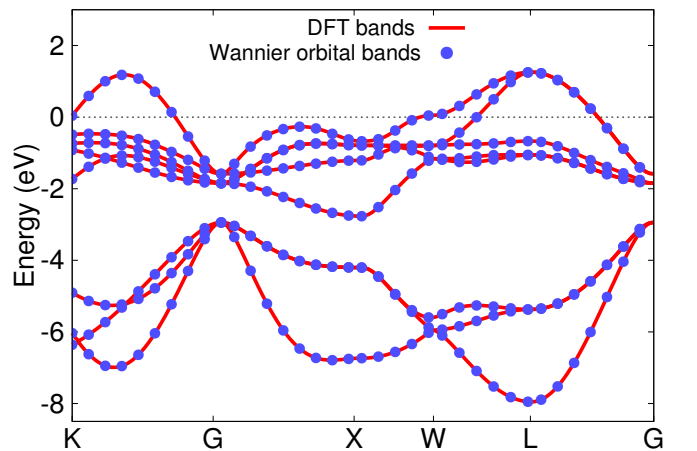


FIG. 1. DFT band structure of NiO (solid line), and reconstructed band structure in Wannier orbital basis (dots). Fermi level is at zero.

In practice we have included 100 empty bands in the DFT ground state calculation. After the Wannier orbital projection,

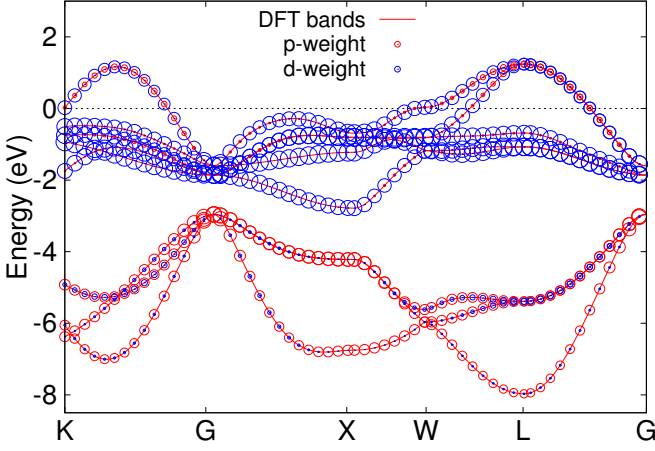


FIG. 2. Band character of NiO from projecting Bloch states on to atomic orbital states. The radius of open circles are proportional to the weight of the atomic states. Fermi level is at zero.

$W_r(\omega = 0)$ is calculated for the dp model by excluding the d - and p -like bands, and for the d - dp model by excluding only d -like bands.

II.D. CBS Approach for Calculating the β Parameter

Complex band structure is the band structure defined on complex values of \vec{k} . The wavefunction transmission decay is always associated with a specific direction in real space, or, equivalently, a specific \vec{k} in reciprocal space. The β parameter is thus a function of \vec{k} . The calculation of the CBS allows us to extract the β -parameter for the four late TMOs that characterizes the decay of nonresonant tunneling current. In this work we study the CBS of these simple materials within the Green's function scheme. This part of the calculation is done on top of DFT+DMFT results. Specifically, after obtaining DMFT self-energy convergence, we use the resulting self-energy expressed in real frequency space to calculate the complex band structure within the correlation subspace. The full Green's function is expressed in the usual way:

$$G(\vec{k}, \omega) = \frac{1}{\omega + \mu - H(\vec{k}) - \Sigma^{DMFT}(\omega)} \quad (11)$$

In Eq.(11), μ is the Fermi level, which is set to zero throughout the calculations. $H(\vec{k})$ is the downfolded Hamiltonian using the Wannier orbital basis. $\Sigma(\omega)$ is the converged DMFT self-energy after analytical continuation. In order to get the CBS (and β) for a specific direction in \vec{k} -space, we make the \vec{k} vector a complex variable by supplying a complex coefficient to the direction of interest. For a given value of ω , one searches for poles of the Green's function $G(\vec{k}, \omega)$ in the plane of the complex coefficient. In practice, we found it convenient to express any \vec{k} vector in the 1st Brillouin zone as $\vec{k} = C_1 \cdot \hat{k}_1 + C_2 \cdot \hat{k}_2 + C_3 \cdot \hat{k}_3$, where \hat{k}_1, \hat{k}_2 and \hat{k}_3 are user-defined constant unit vectors, \hat{k}_1 is *always* the direction in which we

want to study the decay, and \hat{k}_2 and \hat{k}_3 are both in the plane perpendicular to \hat{k}_1 but not necessarily perpendicular to each other. The coefficient C_1 is *always* the supplied complex coefficient, and C_2 and C_3 are real coefficients.

For each given value of ω and fixed values of C_2 and C_3 , the Green's function is considered as a function of C_1 only, i.e. $G(\vec{k}, \omega) = G(C_1)$. We resolve the poles of $G(C_1)$ in a proper area of C_1 plane by finding roots of the equation: $\det[G^{-1}(C_1)] = 0$. The set of roots for different values of ω gives the CBS. Fig.3 shows the complex domain that we are interested in for the case where \hat{k}_1 is chosen to be $\vec{b}_3/|\vec{b}_3|$ and $\hat{k}_2 = \hat{k}_3 = 0$.

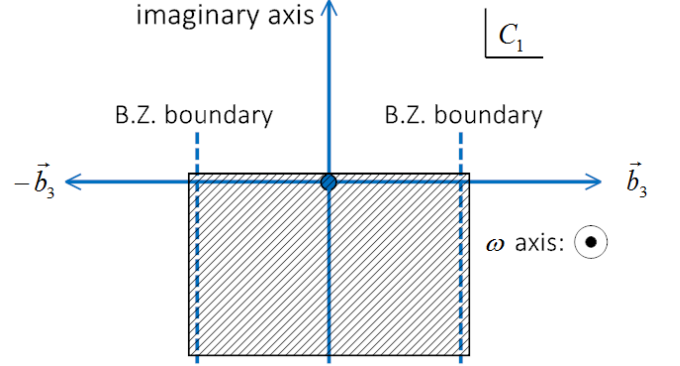


FIG. 3. Area in C_1 plane for the complex band structure of the direction $\hat{k}_1 = \vec{b}_3/|\vec{b}_3|$, where \vec{b}_3 is the reciprocal lattice vector. In practice the area is made a little larger to completely include the real axis and boundaries of the 1st Brillouin Zone, and the $\text{Im}[C_1]$ must cover the range from zero to a negative value whose absolute value is large enough to include a few poles. The plane of $\omega = 0$ denotes the Fermi surface.

For a given direction, there are many complex bands passing through the Fermi surface, and each crossing gives a β value, one identifies the smallest absolute value as the correct β since it corresponds to the longest decay length. In summary, for each $\hat{\mathbf{k}}_\perp$, we calculated the CBS around the Fermi level for each point on a dense grid of (C_2, C_3) to account for different points in $\hat{\mathbf{k}}_\parallel$. The distributions of $\beta(\hat{\mathbf{k}}_\parallel)$ are finally obtained for the three directions: (a) $\hat{\mathbf{k}}_\perp = (\hat{k}_x = 1, \hat{k}_y = 0, \hat{k}_z = 0)$; (b) $\hat{\mathbf{k}}_\perp = (\hat{k}_x = 1, \hat{k}_y = 1, \hat{k}_z = 0)$; (c) $\hat{\mathbf{k}}_\perp = (\hat{k}_x = 1, \hat{k}_y = 1, \hat{k}_z = 1)$, where $(\hat{k}_x, \hat{k}_y, \hat{k}_z)$ is the \mathbf{k} -space Cartesian coordinates. The results are presented in next section.

III. RESULTS AND DISCUSSION

In this section we first report our cRPA calculation of the U matrices, followed by the DFT+DMFT calculation of the band gaps of the four materials. Then the complex band structures based on the DMFT spectral function are presented, and the values of β parameters are extracted from the complex band structures.

III.A. Band Gaps from DFT+DMFT

The direct outputs of the cRPA calculation are the $U_{mm'}^{cRPA}$ and $J_{mm'}^{cRPA}$ matrices. The Coulomb interaction U matrices used in most DMFT literatures are actually combination of the two: $U_{mm'}^{\sigma\sigma} = U_{mm'}^{cRPA} - J_{mm'}^{cRPA}$, $U_{mm'}^{\sigma\bar{\sigma}} = U_{mm'}^{cRPA}$. Our results are listed in the Appendix, following this convention. The values of the interaction strength in both models are close to those in the literature³¹. Here we derived the static Coulomb intra-orbital, inter-orbital and exchange interaction parameters U , U' and J from averaging the matrix elements of U , for easy comparison. It is identified by definition that the diagonal elements of either $U_{mm'}^{cRPA}$ or $J_{mm'}^{cRPA}$ are the intra-orbital elements, and one can take the average value: $U = \frac{1}{5} \text{Tr} U_{mm'}^{cRPA} = \frac{1}{5} \text{Tr} J_{mm'}^{cRPA}$. The inter-orbital interactions are represented as the off-diagonal elements of $U_{mm'}^{cRPA}$, thus $U' = \frac{1}{20} \sum_{m \neq m'} U_{mm'}^{cRPA}$. Similarly the inter-orbital exchange is $J = \frac{1}{20} \sum_{m \neq m'} J_{mm'}^{cRPA}$. The values of U , U' and J are summarized in Table I.

(eV)	NiO	CoO	FeO	MnO
$U, dp \text{ model}$	9.92(10.3)	9.53(9.8)	9.09(9.5)	8.95(9.2)
$U, d-dp \text{ model}$	7.33(7.6)	6.51(6.8)	5.94(6.3)	5.65(6.1)
$U', dp \text{ model}$	8.35(8.6)	8.03(8.1)	7.71(7.9)	7.64(7.7)
$U', d-dp \text{ model}$	5.81(5.9)	5.07(5.2)	4.62(4.8)	4.40(4.6)
$J, dp \text{ model}$	0.78(0.9)	0.75(0.8)	0.70(0.8)	0.66(0.7)
$J, d-dp \text{ model}$	0.77(0.9)	0.73(0.8)	0.68(0.8)	0.64(0.7)

TABLE I. The values of U , U' and J deduced from the cRPA calculation. Values in parenthesis are from Ref.³¹ for the same model construction using a different code based on Maximum Localized Wannier Functions.

The U matrices are used for the subsequent DMFT calculations. The resulting density of states (DOS) and k -resolved spectral function from the DFT+DMFT calculations are presented in Fig.4 and Fig.5 for dp and $d-dp$ models for NiO. The band gaps are measured between the widths at half height of the conduction band and valence band from DOS. The band gap values are listed in Table II. Here we briefly compare to the band gaps obtained from experiments. NiO and MnO have been extensively studied in experiments. The band gap of NiO was experimentally determined to be 3.7-4.5 eV^{32,33}. The experimental values of MnO gap is in the range of 3.6-4.0 eV^{32,34}. The present calculation of the $d-dp$ model are in agreement with experiments for these two materials. Experimental band gap of CoO has quite diverse values. Several experimental reports give a band gap of 2.5-2.8 eV³⁵. Some other studies found much higher values. For example, Kant *et al* reported a 5.4 eV gap based on ellipsometry spectra data³⁶ and Roland *et al* calculated the absorption spectrum from the measured dielectric function, which yields an indirect band gap of 2.8 eV and a direct band gap of 5 eV³⁵. Unfortunately, there are very limited experiments reporting the measured band gaps of FeO. This is because the preparation of a pure FeO sample is difficult due to Fe segregation³⁷. Thus, comparison of theoretical calculation with experimental spectra is very rare. The only reported experimental estimate that

we found is 2.4 eV from an optical absorption measurement³⁷. Overall the $d-dp$ models give smaller band gap than the dp models, and appear to be closer to the range of experimental results. This general feature suggests that, in the context of DFT+DMFT, excluding only the d -like bands in the cRPA calculations should be enough to give accurate screened Coulomb interactions for these materials.

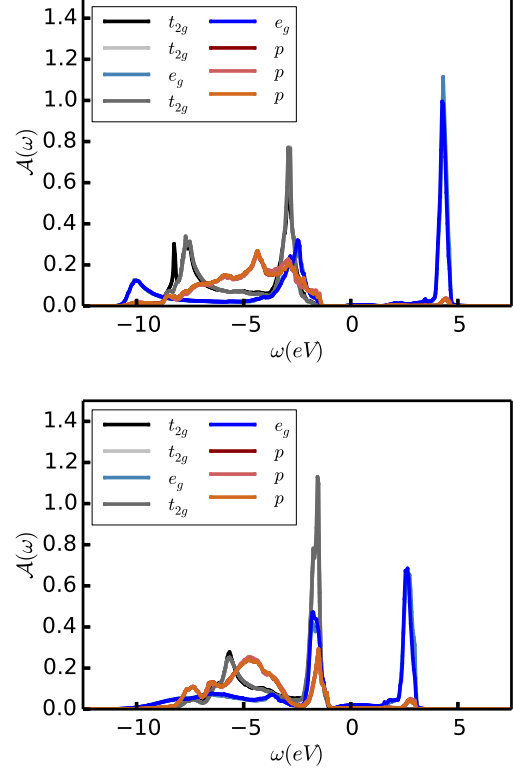


FIG. 4. Density of states of the dp and $d-dp$ models of NiO, from DFT+DMFT calculation.

Band Gap (eV)	NiO	CoO	FeO	MnO
DFT+DMFT, $dp \text{ model}$	6.74	6.63	6.05	6.74
DFT+DMFT, $d-dp \text{ model}$	4.76	3.72	3.37	3.72
Exp(conductivity)	3.7	3.6	n/a	3.8
Exp(XAS-XES)	4.0	2.6	n/a	4.1
Exp(PES-BIS)	4.5	2.5	n/a	3.9
Exp(absorption)	4.0	2.8	2.4	3.6-3.8

TABLE II. The band gaps measured from DFT+DMFT density of states. Sources of the experimental gaps are in text of Sec.III.A.

Comparing the DFT+DMFT method with other manybody calculation methods is far beyond the present work. But at this point we think it's worth mentioning that there are several G_0W_0 studies for these materials. For example calculations based on the HSE03 hybrid functional and G_0W_0 method gave band gaps of 4.7 eV for NiO³⁸ and 3.2-3.4 eV for CoO³⁹. The G_0W_0 calculation based on LDA+U wavefunctions and pure

HSE03 calculation gives smaller band gap of 3.8 and 4.1 eV for NiO³⁸. It may benefit from GW+DMFT calculations to resolve the situation.

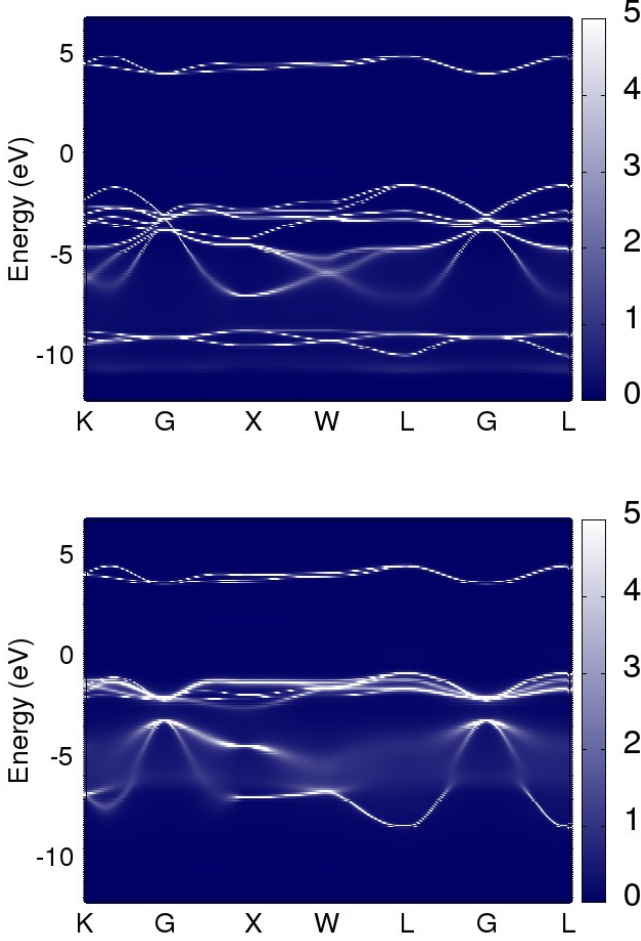


FIG. 5. Spectral functions of the dp and $d-dp$ models of NiO

In our calculation, the value of U matrix is important to yield the correct band gaps for the four materials. We have found that the $d-dp$ model results are in better agreement with existing experiments. The dp model seems to overestimate the band gap, which is the direct consequence of the larger interaction. However, the preference of the $d-dp$ model over the dp model could be more carefully supported by taking into consideration the other related factors. For example, it has been recently proposed that the current cRPA method could be improved by including the Pauli exclusion principle in the formalism, and overall the effect would be a reduction of the interaction strength⁴⁰. There are also other factors within the DMFT calculation, e.g. different double counting methods, that can affect the resulting spectral function. Including those factors is outside the scope of this work. Thus we limit our discussion to be within the original cRPA scheme and with only fully localized limit (FLL) double counting in the DMFT part. We would like to emphasize that, for consistency, one set of projected Wannier orbital basis functions is used in both

the downfolded Hamiltonian $H(k)$ for DMFT and the cRPA-calculated Coulomb interaction U matrices.

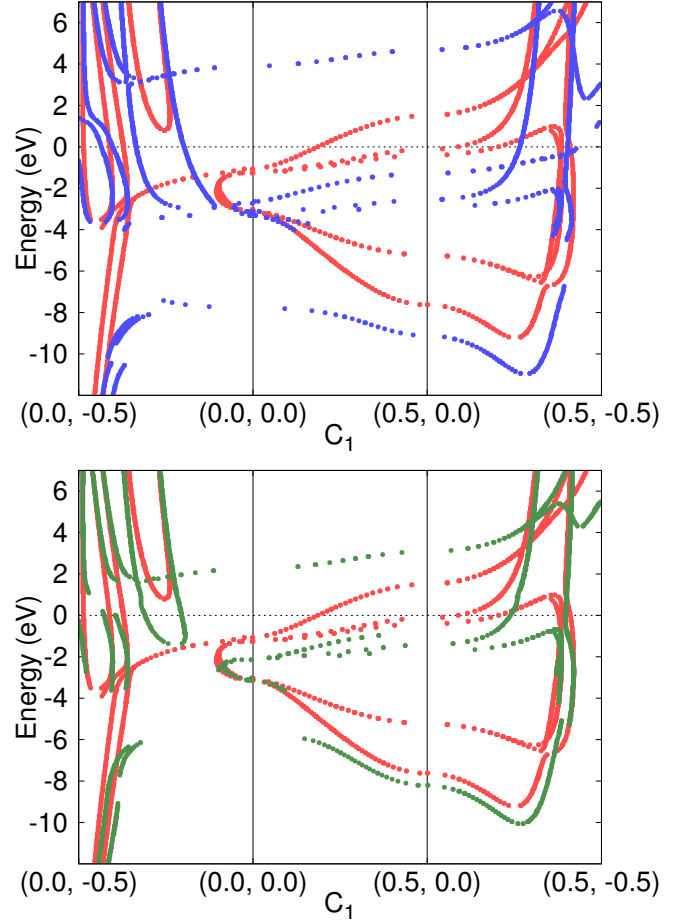


FIG. 6. Complex band structures of NiO, along a path in the C_1 plane and $\hat{\mathbf{k}}_{\perp} = \vec{b}_1/|\vec{b}_1|$. C_2 and C_3 are set to zero. Upper plot: dp model(blue) vs. non-interacting(red). Lower plot: $d-dp$ model(green) vs. non-interacting(red).

III.B. CBS including DMFT self-energy

By including or excluding the impurity self-energy, the CBS or RBS can be obtained from resolving poles of the Green's function, as explained in Section II.D. Fig.6 plots the CBS and RBS for the case of $\hat{\mathbf{k}}_{\perp} = \vec{b}_1/|\vec{b}_1|$ and $C_2=C_3=0$, where \vec{b}_1 is one reciprocal lattice vector of fcc NiO. The CBS of the two models are shown separately in two plots with comparison with the non-interacting case (red dots in both plots). The middle part of Fig.6, $C_1: (0.0, 0.0) \rightarrow (0.5, 0.0)$, corresponds to the path $G \rightarrow L$ in Fig.5. It is clearly seen that there are complex bands crossing the Fermi level in the left part and right part of Fig.6, for both dp and $d-dp$ models. Similar crossings are observed for $C_1: (\alpha, -0.5) \rightarrow (\alpha, 0.0)$, $\alpha \in (0.0, 0.5)$. By observing all of the complex branches crossing the Fermi level in the complex plane containing the direction of interest, we identify the k -point with smallest distance to

the real axis as the β parameter point for that direction of interest. Specifically for the case of Fig.6, β point happens to be the crossing on C_1 : $(0.0, -0.5) \rightarrow (0.0, 0.0)$, *i.e.* the left part in Fig.6.

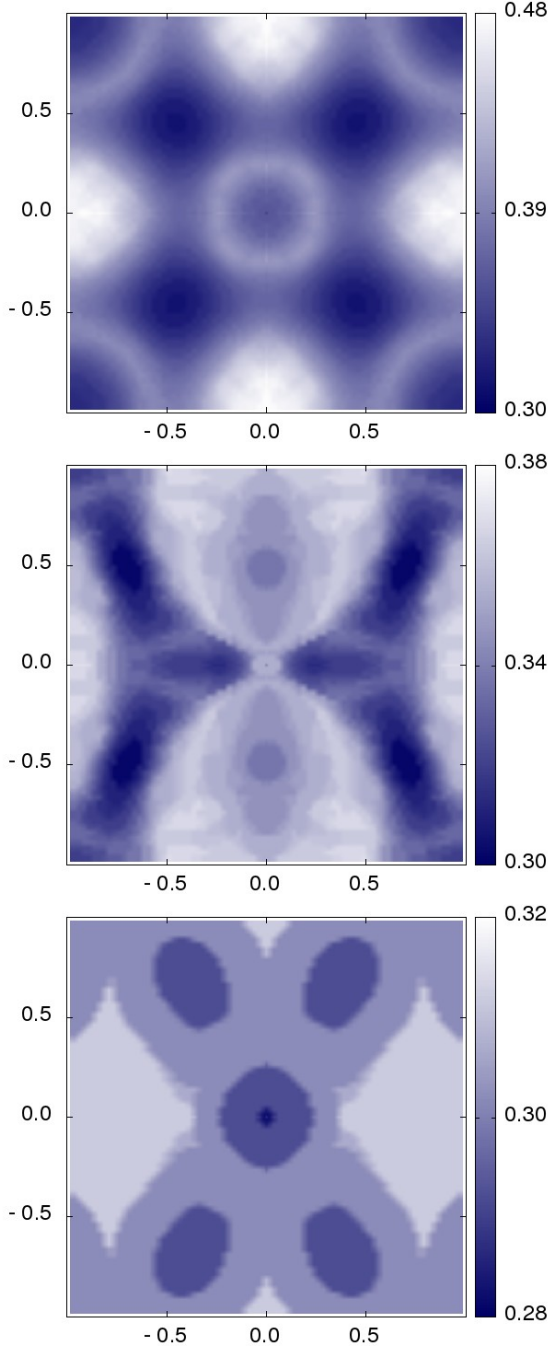


FIG. 7. Distribution of the values of β parameter of NiO, for the decay in the three directions: (1) $\hat{\mathbf{k}}_{\perp} = (0, 0, 1)$, upper plot, (2) $\hat{\mathbf{k}}_{\perp} = (0, 1, 1)/\sqrt{2}$, middle plot and (3) $\hat{\mathbf{k}}_{\perp} = (1, 1, 1)/\sqrt{3}$, lower plot. The in-plane axes are (C_2, C_3) from -1 to +1 to specify $\hat{\mathbf{k}}_{\parallel}$

Particularly, we found that the β parameter does not differ significantly between the two models. For example, the complex branches of $\text{Re}C_1=0.0$ in Fig.6, blue dots and green dots

on the left side, both pass the Fermi surface at about $\text{Im}C_1=-0.2$. The same feature is observed for the three different directions in k -space (defined in next paragraph) of our study. Numerically some regions of the complex and real bands smears out, for example near the G point in energy range from -3 to -7 eV. Such smearing is explained within the quasiparticle picture in which spectral weights have spreads, as seen in the k -resolved spectral Fig.5.

We have performed the calculations for the three directions: (a) $\hat{\mathbf{k}}_{\perp} = (1, 0, 0)$, which is the case of Fig.6; (b) $\hat{\mathbf{k}}_{\perp} = (1, 1, 0)$; and (c) $\hat{\mathbf{k}}_{\perp} = (1, 1, 1)$. We have obtained the k -resolved β distribution as shown in Fig.7. The symmetry of these β distributions are in consistent with the *fcc* NiO crystal symmetry, which makes sense because the single-site DMFT assumes completely localized self-energy. The range of β values are different for the three directions. This observation becomes clearer when we introduce the β -resolved density of state $n(\beta)$ ⁴¹. Ideally $n(\beta)d\beta$ would be the number of "states" with β values in the infinitesimal interval $(\beta, \beta + d\beta)$. In numerical calculations, we resolved 80 grid points within $[0,1]$ for both C_2 and C_3 to calculate β and applied linear interpolation to make the grid 100 times denser. The resulting density is shown in Fig.8. It's clear that the decay parameters are crowded around 0.3 for the $(1,1,1)$ direction, and extends to larger and larger values in $(0,1,1)$ and $(0,0,1)$ directions.

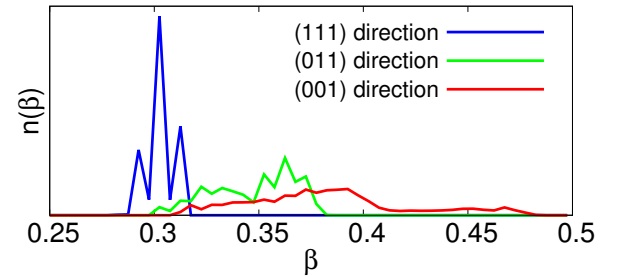


FIG. 8. β -resolved density of state $n(\beta)$ for the three directions in k -space.

If we assume that the electronic states outside the correlation window do not play an important role in the tunneling current, then we can use a simplified model to estimate the transmission probability for these materials. The transmission probability takes the form $T_{\hat{\mathbf{k}}_{\parallel}}(d) = T_0 \cdot \exp(-\beta_{\hat{\mathbf{k}}_{\parallel}} \cdot d)$, where d is the thickness of the tunneling barrier and $\beta_{\hat{\mathbf{k}}_{\parallel}}$ is the density obtained above. The total transmission probability for the direction $\hat{\mathbf{k}}_{\perp}$ is given by:

$$T_{\text{tot}}(d) = \frac{1}{N_{\hat{\mathbf{k}}_{\parallel}}} \sum_{\hat{\mathbf{k}}_{\parallel}} T_{\hat{\mathbf{k}}_{\parallel}}(d) \quad (12)$$

In Fig.9 we plot the relative transmission, $T_{\text{tot}}(d)/T_{\text{tot}}(d=0)$, as function of barrier thickness for the three directions. The

common feature of exponential decay is clear for all three directions. The overall larger values of β in the (0,0,1) direction results in a faster decay than the other two directions, as expected.

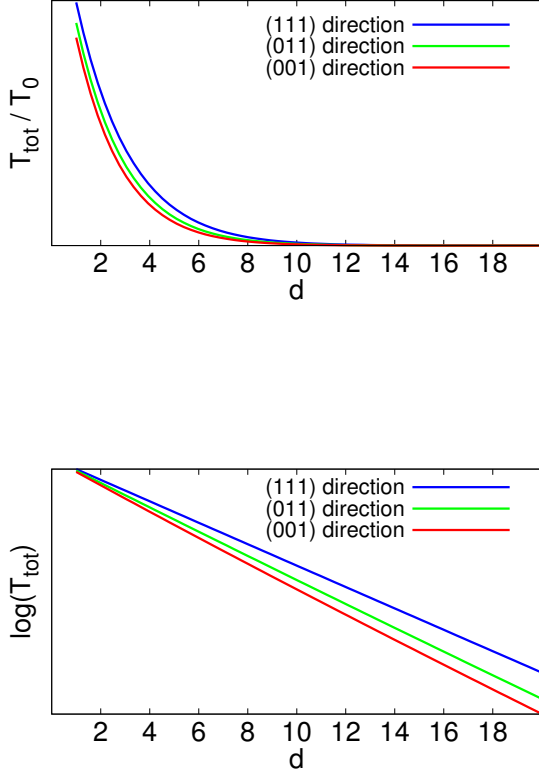


FIG. 9. Upper plot: relative transmission, $T_{\text{tot}}(d)/T_{\text{tot}}(d = 0)$, as function of barrier thickness for the three directions in k -space; Lower plot: Log scale of the upper plot;

IV. CONCLUSION

In summary, we have performed DFT plus single-site DMFT calculation for the four transition metal monoxides, NiO, CoO, FeO and MnO, in the non-spin-polarized phase, and have studied the complex band structure of these materials by including the DMFT self-energy. Both the dp and $d-dp$ models have been investigated, and the corresponding screened Coulomb interaction parameters are calculated from first-principles using the cRPA method. The resulting spectral functions present a clear band gap in both model calculations, improving upon the gapless DFT ground state calculation. By using the full Green's function from DMFT, we have observed different complex band structures for different model constructions. The transmission decay parameter, β , has been calculated from the complex bands for three different directions in k -space to give us insight into the current decay

property for the bulk phase of these materials. We found that the β parameters have very different values and distributions for different directions. In a further study, it would be interesting to observe the β distribution being modified through the use of a cluster-type self-energy $\Sigma(k, \omega)$.

In conclusion, the presented work represents a fully controlled way to study current transport properties of correlated insulators. The main physical features are captured in a parameter-free way. The current approach could also be applied to more complicated structures or lower dimensional cases, as long as the application of single-site DFT+DMFT is justified.

Acknowledgements

This work was supported by the US Department of Energy (DOE), Office of Basic Energy Sciences (BES), under Contract No. DE-FG02-02ER45995. The computation was done using the utilities of the National Energy Research Scientific Computing Center (NERSC).

V. APPENDIX A

The cRPA-calculated U matrices for the two models, dp and $d-dp$, of each of the four materials are listed here. The columns (rows) are ordered, from left to right (up to down): d_{xy} , d_{yz} , $d_{x^2-y^2}$, d_{zx} , d_{z^2} . The values are in unit of eV.

NiO, dp model:

$$U_{mm'}^{\sigma\bar{\sigma}} = \begin{pmatrix} 9.69 & 8.03 & 7.97 & 8.03 & 9.10 \\ 8.03 & 9.69 & 8.82 & 8.03 & 8.25 \\ 7.97 & 8.82 & 10.27 & 8.82 & 8.19 \\ 8.03 & 8.03 & 8.82 & 9.69 & 8.25 \\ 9.10 & 8.25 & 8.19 & 8.25 & 10.27 \end{pmatrix}$$

$$U_{mm'}^{\sigma\sigma} = \begin{pmatrix} 0.00 & 7.21 & 6.97 & 7.21 & 8.66 \\ 7.21 & 0.00 & 8.24 & 7.21 & 7.39 \\ 6.97 & 8.24 & 0.00 & 8.24 & 7.15 \\ 7.21 & 7.21 & 8.24 & 0.00 & 7.39 \\ 8.66 & 7.39 & 7.15 & 7.39 & 0.00 \end{pmatrix}$$

NiO, $d-dp$ model:

$$U_{mm'}^{\sigma\bar{\sigma}} = \begin{pmatrix} 7.29 & 5.67 & 5.42 & 5.67 & 6.48 \\ 5.67 & 7.29 & 6.21 & 5.67 & 5.69 \\ 5.42 & 6.21 & 7.38 & 6.21 & 5.44 \\ 5.67 & 5.67 & 6.21 & 7.29 & 5.69 \\ 6.48 & 5.69 & 5.44 & 5.69 & 7.38 \end{pmatrix}$$

$$U_{mm'}^{\sigma\sigma} = \begin{pmatrix} 0.00 & 4.85 & 4.44 & 4.85 & 6.04 \\ 4.85 & 0.00 & 5.64 & 4.85 & 4.84 \\ 4.44 & 5.64 & 0.00 & 5.64 & 4.47 \\ 4.85 & 4.85 & 5.64 & 0.00 & 4.84 \\ 6.04 & 4.84 & 4.47 & 4.84 & 0.00 \end{pmatrix}$$

CoO, dp model:

$$U_{mm'}^{\sigma\bar{\sigma}} = \begin{pmatrix} 9.27 & 7.70 & 7.69 & 7.70 & 8.73 \\ 7.70 & 9.27 & 8.47 & 7.70 & 7.95 \\ 7.69 & 8.47 & 9.92 & 8.47 & 7.93 \\ 7.70 & 7.70 & 8.47 & 9.27 & 7.95 \\ 8.73 & 7.95 & 7.93 & 7.95 & 9.92 \end{pmatrix}$$

$$U_{mm'}^{\sigma\sigma} = \begin{pmatrix} 0.00 & 6.92 & 6.73 & 6.92 & 8.30 \\ 6.92 & 0.00 & 7.91 & 6.92 & 7.12 \\ 6.73 & 7.91 & 0.00 & 7.91 & 6.93 \\ 6.92 & 6.92 & 7.91 & 0.00 & 7.12 \\ 8.30 & 7.12 & 6.93 & 7.12 & 0.00 \end{pmatrix}$$

CoO, $d-dp$ model:

$$U_{mm'}^{\sigma\bar{\sigma}} = \begin{pmatrix} 6.47 & 4.94 & 4.71 & 4.94 & 5.68 \\ 4.94 & 6.47 & 5.43 & 4.94 & 4.96 \\ 4.71 & 5.44 & 6.57 & 5.44 & 4.74 \\ 4.94 & 4.94 & 5.44 & 6.47 & 4.96 \\ 5.68 & 4.96 & 4.74 & 4.96 & 6.57 \end{pmatrix}$$

$$U_{mm'}^{\sigma\sigma} = \begin{pmatrix} 0.00 & 4.16 & 3.78 & 4.16 & 5.25 \\ 4.16 & 0.00 & 4.89 & 4.16 & 4.15 \\ 3.78 & 4.89 & 0.00 & 4.89 & 3.82 \\ 4.16 & 4.16 & 4.89 & 0.00 & 4.15 \\ 5.25 & 4.15 & 3.82 & 4.15 & 0.00 \end{pmatrix}$$

FeO, dp model:

$$U_{mm'}^{\sigma\bar{\sigma}} = \begin{pmatrix} 8.91 & 7.49 & 7.53 & 7.49 & 8.40 \\ 7.49 & 8.91 & 8.18 & 7.49 & 7.75 \\ 7.53 & 8.18 & 9.59 & 8.18 & 7.79 \\ 7.49 & 7.49 & 8.18 & 8.91 & 7.75 \\ 8.40 & 7.75 & 7.79 & 7.75 & 9.59 \end{pmatrix}$$

$$U_{mm'}^{\sigma\sigma} = \begin{pmatrix} 0.00 & 6.76 & 6.64 & 6.76 & 7.98 \\ 6.76 & 0.00 & 7.65 & 6.76 & 6.98 \\ 6.64 & 7.65 & 0.00 & 7.65 & 6.89 \\ 6.76 & 6.76 & 7.65 & 0.00 & 6.98 \\ 7.98 & 6.98 & 6.89 & 6.98 & 0.00 \end{pmatrix}$$

FeO, $d-dp$ model:

$$U_{mm'}^{\sigma\bar{\sigma}} = \begin{pmatrix} 5.89 & 4.50 & 4.33 & 4.50 & 5.13 \\ 4.50 & 5.89 & 4.93 & 4.50 & 4.53 \\ 4.33 & 4.93 & 6.02 & 4.93 & 4.35 \\ 4.50 & 4.50 & 4.93 & 5.89 & 4.53 \\ 5.13 & 4.53 & 4.35 & 4.53 & 6.02 \end{pmatrix}$$

$$U_{mm'}^{\sigma\sigma} = \begin{pmatrix} 0.00 & 3.78 & 3.47 & 3.78 & 4.71 \\ 3.78 & 0.00 & 4.40 & 3.78 & 3.78 \\ 3.47 & 4.40 & 0.00 & 4.40 & 3.52 \\ 3.78 & 3.78 & 4.40 & 0.00 & 3.78 \\ 4.71 & 3.78 & 3.52 & 3.78 & 0.00 \end{pmatrix}$$

MnO, dp model:

$$U_{mm'}^{\sigma\bar{\sigma}} = \begin{pmatrix} 8.68 & 7.34 & 7.39 & 7.34 & 8.18 \\ 7.34 & 8.68 & 7.99 & 7.34 & 7.59 \\ 7.39 & 7.99 & 9.34 & 7.99 & 7.65 \\ 7.34 & 7.34 & 7.99 & 8.68 & 7.59 \\ 8.18 & 7.59 & 7.65 & 7.59 & 9.34 \end{pmatrix}$$

$$U_{mm'}^{\sigma\sigma} = \begin{pmatrix} 0.00 & 6.65 & 6.56 & 6.65 & 7.78 \\ 6.65 & 0.00 & 7.47 & 6.65 & 6.87 \\ 6.56 & 7.47 & 0.00 & 7.47 & 6.80 \\ 6.65 & 6.65 & 7.47 & 0.00 & 6.87 \\ 7.78 & 6.87 & 6.80 & 6.87 & 0.00 \end{pmatrix}$$

MnO, $d-dp$ model:

$$U_{mm'}^{\sigma\bar{\sigma}} = \begin{pmatrix} 5.59 & 4.28 & 4.13 & 4.28 & 4.86 \\ 4.28 & 5.59 & 4.68 & 4.28 & 4.31 \\ 4.13 & 4.68 & 5.73 & 4.68 & 4.17 \\ 4.28 & 4.28 & 4.68 & 5.59 & 4.31 \\ 4.86 & 4.31 & 4.17 & 4.31 & 5.73 \end{pmatrix}$$

$$U_{mm'}^{\sigma\sigma} = \begin{pmatrix} 0.00 & 3.60 & 3.33 & 3.60 & 4.46 \\ 3.60 & 0.00 & 4.18 & 3.60 & 3.61 \\ 3.33 & 4.18 & 0.00 & 4.18 & 3.38 \\ 3.60 & 3.60 & 4.18 & 0.00 & 3.61 \\ 4.46 & 3.61 & 3.38 & 3.61 & 0.00 \end{pmatrix}$$

* current address: Cognitive Computing and Industry Solutions, IBM Research, Saumerstrasse 4, 8803 Rueschlikon, Switzerland

† Contact Email: cheng@qtp.ufl.edu; Tel: 352-392-6256

- ¹ J. K. Tomfohr and O. F. Sankey, Phys. Rev. B **65**, 245105 (2002).
- ² A. Ferretti, G. Mallia, L. Martin-Samos, G. Bussi, A. Ruini, B. Montanari, and N. M. Harrison, Phys. Rev. B **85**, 235105 (2012).
- ³ J. Zaanen, G. A. Sawatzky, and J. W. Allen, Phys. Rev. Lett. **55**, 418 (1985).
- ⁴ M. V.I. Anisimov and E.Z. Kurmaev, J. Phys.: Condens. Matter **2**, 3973 (1990).
- ⁵ A. B. Shick, A. I. Liechtenstein, and W. E. Pickett, Phys. Rev. B **60**, 10763 (1999).
- ⁶ S. S. W. S. Maekawa, T. Tohyama and G. Khaliullin, (2004).
- ⁷ R. W. Yang, Oxford University Press (1994).
- ⁸ U. von Barth and L. Hedin, Journal of Physics C: Solid State Physics **5**, 1629 (1972).
- ⁹ D. Korotin, A. V. Kozhevnikov, S. L. Skornyakov, I. Leonov, N. Binggeli, V. I. Anisimov, and G. Trimarchi, The European Physical Journal B **65**, 91 (2008).
- ¹⁰ M. Karolak, G. Ulm, T. Wehling, V. Mazurenko, A. Poteryaev, and A. Lichtenstein, Journal of Electron Spectroscopy and Related Phenomena **181**, 11 (2010), proceedings of International Workshop on Strong Correlations and Angle-Resolved Photoemission Spectroscopy 2009.
- ¹¹ M. Cyrot, Journal de Physique **33**, 125 (1972).
- ¹² O. Tjernberg, S. Söderholm, G. Chiaia, R. Girard, U. O. Karlsson, H. Nylén, and I. Lindau, Phys. Rev. B **54**, 10245 (1996).
- ¹³ F. Aryasetiawan, M. Imada, A. Georges, G. Kotliar, S. Biermann, and A. I. Lichtenstein, Phys. Rev. B **70**, 195104 (2004).
- ¹⁴ N. F. Mott and R. Peierls, Proceedings of the Physical Society **49**, 72 (1937).
- ¹⁵ N. F. Mott, Proceedings of the Physical Society. Section A **62**, 416 (1949).
- ¹⁶ A. Georges, G. Kotliar, W. Krauth, and M. J. Rozenberg, Rev. Mod. Phys. **68**, 13 (1996).
- ¹⁷ W. R. L. Lambrecht and O. K. Andersen, Phys. Rev. B **34**, 2439 (1986).
- ¹⁸ N. Marzari and D. Vanderbilt, Phys. Rev. B **56**, 12847 (1997).
- ¹⁹ N. Marzari, A. A. Mostofi, J. R. Yates, I. Souza, and D. Vanderbilt, Rev. Mod. Phys. **84**, 1419 (2012).
- ²⁰ J. Hubbard, Proceedings of the Royal Society of London A: Mathematical, Physical and Engineering Sciences **276**, 238 (1963), <http://rspa.royalsocietypublishing.org/content/276/1365/238.full.pdf>.
- ²¹ B. A. Altland, Cambridge University Press (2006).
- ²² E. Gull, A. J. Millis, A. I. Lichtenstein, A. N. Rubtsov, M. Troyer, and P. Werner, Rev. Mod. Phys. **83**, 349 (2011).
- ²³ P. Staar, T. Maier, and T. C. Schulthess, Phys. Rev. B **88**, 115101 (2013).
- ²⁴ E. Gull, P. Staar, S. Fuchs, P. Nukala, M. S. Summers, T. Pruschke, T. C. Schulthess, and T. Maier, Phys. Rev. B **83**, 075122 (2011).
- ²⁵ P. Staar, B. Ydens, A. Kozhevnikov, J.-P. Locquet, and T. Schulthess, Phys. Rev. B **89**, 245114 (2014).
- ²⁶ F. Aryasetiawan, K. Karlsson, O. Jepsen, and U. Schönberger, Phys. Rev. B **74**, 125106 (2006).
- ²⁷ M. Petersilka, U. J. Gossmann, and E. K. U. Gross, Phys. Rev. Lett. **76**, 1212 (1996).
- ²⁸ A. Kozhevnikov, A. G. Eguiluz, and T. C. Schulthess, 2010 ACM/IEEE International Conference for High Performance Computing, Networking, Storage and Analysis, 1 (2010).
- ²⁹ M. Petersilka, U. J. Gossmann, and E. K. U. Gross, Phys. Rev. Lett. **76**, 1212 (1996).
- ³⁰ L. Vaugier, H. Jiang, and S. Biermann, Phys. Rev. B **86**, 165105 (2012).
- ³¹ R. Sakuma and F. Aryasetiawan, Phys. Rev. B **87**, 165118 (2013).
- ³² R. J. Powell and W. E. Spicer, Phys. Rev. B **2**, 2182 (1970).
- ³³ G. A. Sawatzky and J. W. Allen, Phys. Rev. Lett. **53**, 2339 (1984).
- ³⁴ G. W. Pratt and R. Coelho, Phys. Rev. **116**, 281 (1959).
- ³⁵ R. Gillen and J. Robertson, Journal of Physics: Condensed Matter **25**, 165502 (2013).
- ³⁶ C. Kant, F. Mayr, T. Rudolf, M. Schmidt, F. Schrettle, J. Deisenhofer, and A. Loidl, The European Physical Journal Special Topics **180**, 43 (2009).
- ³⁷ H. Bowen, D. Adler, and B. Auker, Journal of Solid State Chemistry **12**, 355 (1975).
- ³⁸ S. V. Faleev, M. van Schilfgaarde, and T. Kotani, Phys. Rev. Lett. **93**, 126406 (2004).
- ³⁹ C. Rödl, F. Fuchs, J. Furthmüller, and F. Bechstedt, Phys. Rev. B **79**, 235114 (2009).
- ⁴⁰ H. Shinaoka, M. Troyer, and P. Werner, Phys. Rev. B **91**, 245156 (2015).
- ⁴¹ P. Mavropoulos, N. Papanikolaou, and P. H. Dederichs, Phys. Rev. Lett. **85**, 1088 (2000).